

A Physical Background Model for the Fermi Gamma-ray Burst Monitor

B. Biltzinger, F. Kunzweiler, J. Greiner, K. Toelge*, and J. Michael Burgess

Max-Planck-Institut für Extraterrestrische Physik, Giessenbachstrasse 1, 85748 Garching, Germany.

Received 18 December, 2019; accepted 22 May, 2020

ABSTRACT

We present the first physically motivated background model for the Gamma-Ray Burst Monitor (GBM) onboard the Fermi satellite. Such a physically motivated background model has the potential to significantly improve the scientific output of Fermi/GBM, as it can be used to improve the background estimate for spectral analysis and localization of Gamma-Ray Bursts (GRBs) and other sources. Additionally, it can also lead to detections of new transient events, since long/weak or slowly rising ones do not activate one of the existing trigger algorithms. In this paper we show the derivation of such a physically motivated background model, which includes the modeling of the different background sources and the correct handling of the response of GBM. While the goal of the paper is to introduce the model rather than developing a transient search algorithm, we demonstrate the ability of the model to fit the background seen by GBM by showing four applications, namely (1) for a canonical GRB, (2) for the ultra-long GRB 091024, (3) for the V404 Cygni outburst in June 2015, and (4) the ultra-long GRB 130925A.

Key words. methods: data analysis – methods: statistical – gamma rays: general – instrumentation: detectors

1. Introduction

The background seen by astrophysical instruments can be very hard to model, as it normally contains a plethora of unmodeled sources, instrumental background, and general unknowns. Nevertheless, these background signals can contain information which, when modeled, can be extracted for scientific study. For instruments with the ability to spatially separate source and background via e.g. focusing techniques, the characterization of background signals can be simple, at least in the sense that spatially distinct sources of background emission can readily be identified. When an instrument lacks imaging capabilities in the classical sense, i.e. its data are all-sky light curves with sources superimposed upon each other, modeling and separation of background sources must rely on temporal information such as the location of the instrument or viewing direction with time. Then, sources of background emission can be modeled, and pushed through this temporal response of the instrument.

An instrument which is part of the described class of non-imaging instruments is the Gamma-ray Burst Monitor (GBM). GBM is one of two instruments that are part of the Fermi Gamma-Ray Space Telescope which was launched in 2008 into a low-Earth orbit. It consists of 12 sodium iodide (NaI) and 2 bismuth germanate (BGO) detectors, pointing in different directions (see Fig. 1). GBM has an all-sky coverage, except for the part that is occulted by the Earth. The detectors nominally cover an energy interval from 8 keV to 1 MeV for the NaI detectors and 150 keV to 40 MeV for the BGO detectors (Meegan et al. 2009). GBM is used to detect and spectrally analyze transient events. It provides an extension of the energy range over which transient events can be observed below the

the Large Area Telescope (LAT) energy range (which covers 20 MeV to 300 GeV); also it allows fast on-board localization of transients, to point the LAT towards the transient event to detect potential high-energy delayed emission (Meegan et al. 2009). As a non-imaging instrument, GBM is inundated with an all-sky background composed of several constant and temporally evolving sources. Thus, for the identification of temporal transients such as GRBs, GBM relies on the ability to separate source and background in any analysis. The classical approach in estimating the background temporally and spectrally is to identify off-source regions in time and fit smooth functions such as polynomials to each Pulse Height Analysis (PHA) channel's temporally evolving signal. Then, the estimated model is extrapolated into the on-source region, thus providing an estimate for the background in that time interval (Pendleton et al. 1999; Greiner et al. 2016).

This classical approach is suitable for transient events which are short with respect to the typical temporal variation of the background (about 10 min.), but can be very problematic for long duration events, as the background extrapolation can be poor and inaccurate due to non-polynomial variations in the signal. Moreover, assuming independent temporal variations for each channel allows for a high degree of freedom that is unlikely to exist. An alternative approach is to construct a background model from physical components, that evolve temporally and spatially. Such a model can be complex, due to the many different background components, which explains that after 12 years of operation of GBM and 28 years after the CGRO/BATSE observations, there is still no properly working physical model to describe the background of GBM.

Some empirical attempts have been made in the past: (1) Szécsi et al. (2013) fit the background around trigger times of GBM with separate polynomials (up to third order) to differ-

* Present address: Capgemini Nederland B.V., Reykjavikplein 1, 3543 KA Utrecht, Netherlands

ent quantities like the angle between the detector and the Earth, forming a geometrical background model. But this approach gives the fit a lot of freedom as it has many free unbound parameters, introduces ambiguity between the different polynomials and does not use physical information of the sources that create the background. Another work that used the background seen by GBM was done by (2) Horiuchi et al. (2015). In this work they searched for decay lines of sterile neutrinos in the background spectrum of GBM. They used data cuts to get rid of most of the background contamination from e.g. cosmic rays and the Earth Albedo, but did not try to model all the background sources. (3) Fitzpatrick et al. (2012) used the fact that the detectors of GBM, in most cases, are at the same geographical coordinates and point to the same position in the sky every 30th orbit. Thus, they assume that the background at time T should be the same as at time $T \pm 30$ orbits. This is a purely empirical method that for example breaks down, like stated in Fitzpatrick et al. (2012), when there is an Autonomous Repoint Request (ARR) or when due to varying solar activity the particle flux changes or the Earth's magnetic field is compressed. An ARR causes the Fermi satellite to slew, to point the LAT towards a GRB. If this happens, the pointing direction of the GBM detectors will not be the same 30 orbits later.

We wanted to build a predictive background model with a minimum number of free parameters, that incorporates the physics of the source types and the response of the GBM detectors. Such a model should only fit the background and not also (long or slowly varying) transient signals, and should allow us to determine the individual contributions of the different background sources. The model presented herein treats all its components physically except the cosmic ray background, which is explained in subsection 3.3.5. One possible future application for a physically motivated background model could be the possibility to detect events with slow raising count rates (e.g. ultra-long GRBs). Herein, we show some examples of the background seen by GBM in Sec. 2, describe the setup up of such a physically motivated model in Sec. 3, and show results for the ultra-long GRB 091024, the 2015 V404 Cygni outburst and GRB 110920A in Sec. 4.

2. GBM and its Background

GBM converts detected photon events into 128 Pulse Height Analysis (PHA) channels according to the 'height' of the electronic signal at the end of the photo-multiplier tube. These signals are then stored as single events with time tags and the corresponding PHA channel number in the Time-Tagged Events (TTE) data files, but also binned in 8 second time bins with full spectral resolution of 128 PHA channels in the CSPEC data files and with 256 ms time bins with a reduced spectral resolution of only 8 PHA channels in the CTIME data files. The continuous TTE data exist only since 2010 (Meegan et al. 2009).

The background seen by the individual detectors of GBM (see Fig. 1) is a superposition of several different background sources, whose contributions to the total background are strongly dependent on the energy and the orientation of the detectors with respect to the position of the background sources (more details about the different background sources will be described in Sec. 3.3). Since the off-axis sensitivity is energy-dependent, the same photon spectrum will result in different count spectra depending on the orientation of the detector with respect to the source position. The dependence on the orientation leads to different background variations for different detectors in the same recon-

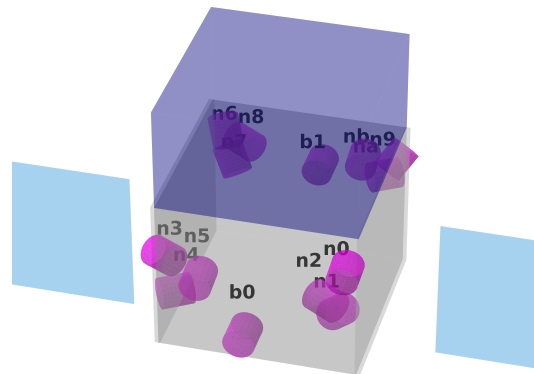


Fig. 1: Schematic picture of the setup of GBM on board of the Fermi satellite. It shows the mounting points and pointing directions for all 14 detectors that are part of GBM. Additionally the satellite base is colored gray, the LAT dark blue and the solar panels light blue.

structed energy range, while the dependence on the energy leads to different background variations for the same detector but different reconstructed energy ranges. This is shown in Fig. 2 and 3. The background model needs to be capable to explain these different backgrounds for different detector orientations and PHA channels.

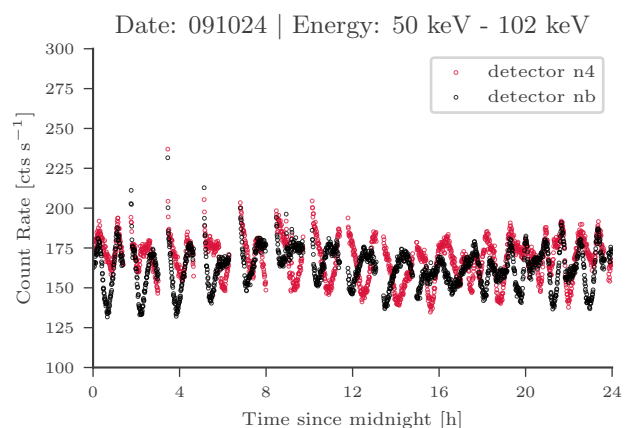


Fig. 2: Background variation at a binning of 15 seconds for the date 24/10/2009 for the two detectors n4 (red circles) and nb (black circles) covering the same reconstructed energy range 50 keV to 102 keV. The time variation of the background is completely different for the two detectors.

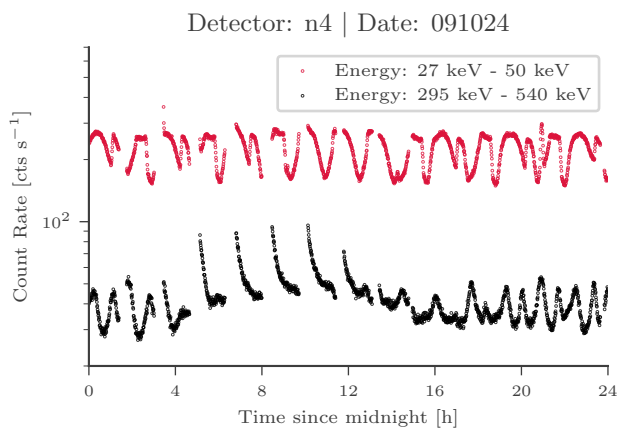


Fig. 3: Background variation at a binning of 15 seconds for the date 24/10/2009 for the detector n4 and for the two reconstructed energy ranges 27 keV to 50 keV (red circles) and 295 keV to 540 keV (black circles). The time variation of the background is completely different for the two energy ranges.

3. Model

3.1. Response

For spectral instruments with large energy dispersion like GBM, modeling the response is crucial for any physical interpretation of the data. The response gives the effective area seen by a photon with a given energy E_{ph} to be detected in one of the detector's PHA channels E_{det} , and therefore connects the physical spectrum of the source with the count rates in the PHA channels. The effects that are incorporated in the response include on the single detector level the geometry of the scintillation crystal, energy dispersion, partial energy deposition of the photons in the crystal and absorption of photons by the detector housing and photo-multiplier tubes attached to the crystal. Additionally, on the satellite level, shielding by other components of the satellite and other detectors is taken into account (see Fig. 4). The response is therefore a function of the position of a source in the satellite frame, the energy of the incoming photon and the PHA channel in which the photon is detected (Kippen et al. 2007).

Each PHA channel has an associated reconstructed energy range, but due to energy dispersion and partial energy deposition of the photon in the crystal this does not imply that all photons detected in this PHA channel have a physical energy within the reconstructed energy range associated to this PHA channel.

The connection of the physical spectrum F [photons $\text{cm}^{-2} \text{s}^{-1}$] and the detected count rate spectrum D [counts s^{-1}] via the response R is given in Eq. 1.

$$D(E_{\text{det}}) = \int dE_{\text{ph}} R(E_{\text{ph}}, E_{\text{det}}, \phi_{\text{source}}, \theta_{\text{source}}) \cdot F(E_{\text{ph}}) \quad (1)$$

The quantities ϕ_{source} and θ_{source} define the position of the source in the satellite frame, with θ_{source} being the zenith angle and $+\phi_{\text{source}}$ the azimuth angle measured from the pointing direction of the b0 detector.

To determine the detector response matrix (DRM), an on-ground calibration of GBM was performed (Bissaldi et al.

2009). We used the Python package `gbm_drm_gen`¹ to get the DRMs. The package `gbm_drm_gen` uses the responses generated via simulation to match the calibration of GBM. With its help one can calculate the DRMs for user defined energy bins of the incoming photons, detector PHA channels and positions of the source (see Fig. 5) (Burgess et al. 2018; Burgess 2019; Berlato et al. 2019).

3.2. Response Implementation

In the physical background model the temporally changing responses for point sources (e.g the Sun) and for extended sources (e.g. Cosmic Gamma-ray Background) are calculated to get the correct influence of these sources on the count rates. The implementation of the response for a point sources is, with the help of the `gbm_drm_gen` package, straightforward:

1. Calculate the position of the point source in the satellite frame for several times with an appropriate time resolution (computation time vs. accuracy of interpolation in step 4).
2. Use the `gbm_drm_gen` package to get the DRMs for the different positions.
3. Convolve the assumed spectrum with the DRMs to get the expected count rates in the different PHA channels.
4. Interpolate between the times for which the point source position was calculated.

The use of an interpolation in time in the last step will of course introduce a systematic error in our analysis. In our implementation, 800 time steps are used for one day which results in one time step every 108 seconds. In this short time the direction of the point source will move only very little in the satellite coordinate frame. Therefore the response change between two time steps is very small which is why the introduced systematic error is small. There are some regions of the GBM response with fast changes for similar directions of the incident photon, which are caused by some parts of the satellite like the LAT radiators. This may introduce a larger error at these times, but we checked that the results do not change if we make the time steps smaller. For the extended sources this procedure has to be modified, as the response is a function of the position of the source in the satellite frame and extended sources cover a range of positions. The formula to connect the flux F [photons $\text{cm}^{-2} \text{s}^{-1} \text{sr}^{-1}$] of the extended sources and the detected count rate spectrum D [counts s^{-1}] is given by

$$D(E_{\text{det}}) = \int \int dE_{\text{ph}} d\Omega R(E_{\text{ph}}, E_{\text{det}}, \phi, \theta) \cdot F(E_{\text{ph}}) \cdot f(\phi, \theta), \quad (2)$$

where $f(\phi, \theta)$ is the occlusion function

$$f(\phi, \theta) = \begin{cases} 1, & \text{if the point is occulted by the source} \\ 0, & \text{otherwise.} \end{cases} \quad (3)$$

For a point source $f(\phi, \theta) = \delta(\phi - \phi_{\text{source}})\delta(\theta - \theta_{\text{source}})$, with which Eq. 2 simplifies to Eq. 1.

To get the expected count rate spectrum of an extended source, the following procedure is applied:

1. Build a grid with N_{grid} equally distributed points on a unit sphere around the detector in the satellite frame.

¹ https://github.com/mpe-heg/gbm_drm_gen/

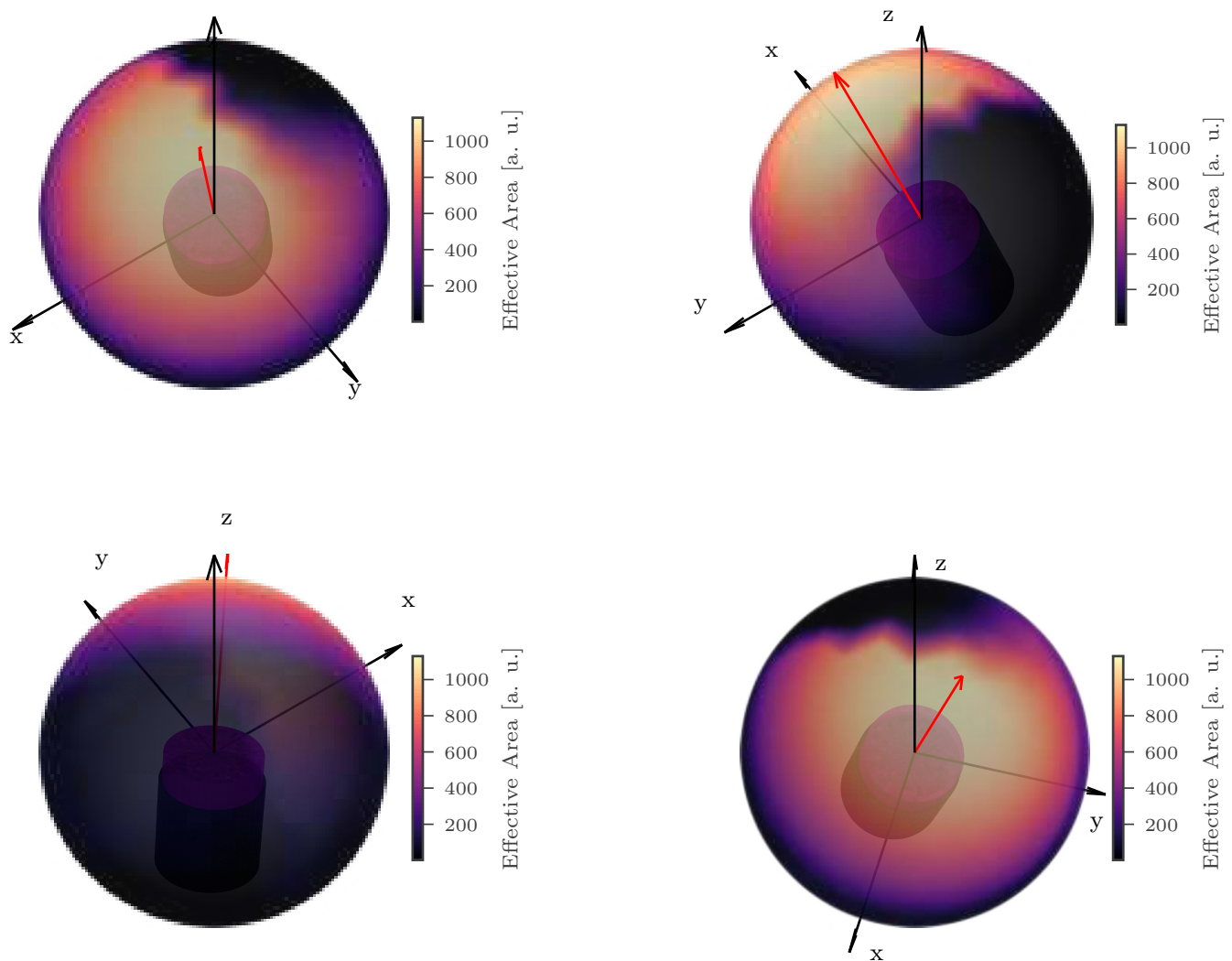


Fig. 4: Effective area seen by a photon with energy 38 keV to be detected in the reconstructed energy channel 2 (CTIME) for different arrival directions on a unit sphere around detector n0 for four different viewing directions on the sphere. The red arrow marks the line of sight of the detector n0 (optical axis), the dark cylinder symbolizes the detector housing and the magenta cylinder the detector crystal. The influence of the LAT is clearly visible in the upper left plot, as it cuts away the effective area on one side of the line of sight. The coordinate system is defined such that the z-axis is the pointing direction of the LAT and the x-axis points along the normal of the satellite side on which the b0 detector is mounted. Responses generated with `gbm_drm_gen` (Burgess et al. 2018; Burgess 2019; Berlato et al. 2019).

2. For each of these points, calculate the DRM with the `gbm_drm_gen` package.
3. Calculate the region covered by the source in the satellite frame for several times with appropriate time resolution (balancing computation time with accuracy of the interpolation in step 6).
4. Sum the responses of the relevant grid points and multiply the result by the solid angle that every point covers ($\frac{4\pi}{N_{\text{grid}}}$ sr) to get an effective response.
5. Convolve the assumed spectrum through the effective response to get the expected count rates in the different PHA channels.
6. Interpolate between the times for which the count rate was calculated.

With the response effects for point sources and extended sources implemented, we can predict the count rate spectrum for any given physical spectrum of any source.

The intense flux of photons from a GRB scatters of the Earth's atmosphere and produce a secondary, weaker flux of photons which can be detected by GBM. Indeed all high-energy radiation can produce such a secondary flux, but at levels far below that of a GRB; therefore, we neglect atmospheric scattering from non-GRB sources in this work.

3.3. Background sources

Our model incorporates 6 components which will be describes in this subsection. We start with the simplest model of a constant background and then adding more components one at a time. For

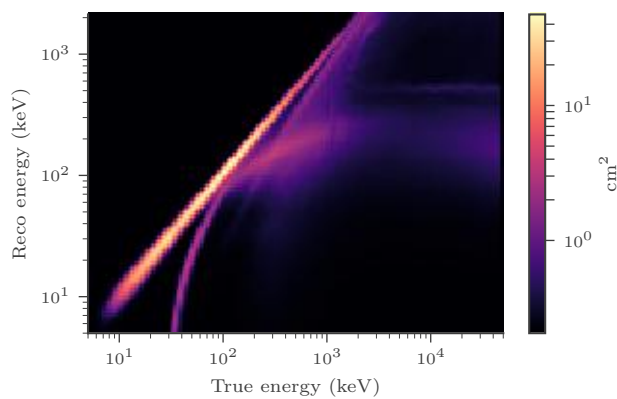


Fig. 5: Example response that shows the effective area for different photon energies to be detected in the PHA channels with associated reconstructed energy. Figure created with the `gbm_drm_gen` package (Hoover et al. 2005; Burgess 2019).

each step we show a fit of the model with the introduced background components to the data of detector n6 for 26/10/2009 between 102 and 295 keV reconstructed energy, showing the improvement we can get by adding the different components to the model. The used components can be categorized into two main classes: The photon and the charged particle background components. The first class is characterized by the components producing a photon spectrum, which is measured by the GBM detectors directly. Members of this class are the Earth Albedo, the Cosmic Gamma-ray Background (CGB), point sources as well as the Sun. In the second class, containing cosmic rays and the South Atlantic Anomaly, charged particles alter the background due to excitation of the satellites atoms or via direct energy deposit in the detectors.

3.3.1. Constant Background

The most intuitive model is that of a constant background which is shown in Fig. 6 plus gaps during every South Atlantic Anomaly (SAA) transition when the detectors are shut down.

When building a physically motivated background model for GBM, for example in order to detect new sources, it is reasonable to start by fitting for the sharply peaked and rapidly decaying signal that occurs after the exits of the South Atlantic Anomaly. This is our first extension to the constant background model.

3.3.2. South Atlantic Anomaly

There are two regions in the Earth's magnetic field which have the right properties to permanently trap large densities of charged particles (mostly protons and electrons) in radiation belts. These two regions are called inner and outer Van-Allen Belts and both lie, outside of the SAA, well above Fermi's orbit, which has an altitude of about 550 km, with the inner Van Allen belt being located between 1000 and 6000km (van Allen & Frank 1959; da Silva & Rocco 2017; Ganushkina et al. 2011).

The South Atlantic Anomaly (SAA) is a region located over the South Atlantic, where the Earth's magnetic field is significantly weaker (Schaefer et al. 2016). This originates from an offset of the dipole which approximates Earth's magnetic field

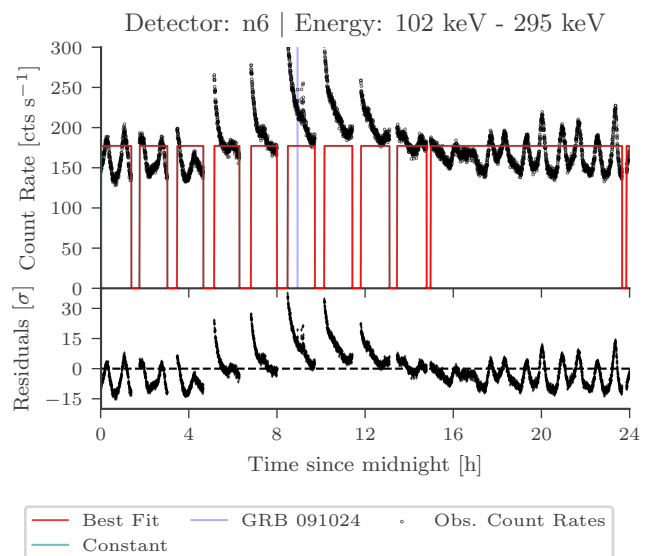


Fig. 6: Fit of a constant line to the data of detector n4 and the energy of 295 keV - 540 keV of day 26/01/2015. The count rate of the model has been set to zero during the SAA passage where the detectors are turned off. The GBM trigger time for GRB 091024 is marked by a cyan line.

and causes the inner Van Allen belt to bend towards the Earth at the position of the SAA (Mozzoni 2007) and reaching an altitude as low as 100 km that therefore intersects Fermi's orbit at 550 km. In order to protect the detectors from damage caused by the high flux of charged particles, the detectors are routinely shut down when the satellite crosses the SAA. Nevertheless, the satellite and detector material undergo nuclear excitation by collision with the charged particles and subsequently photons are produced by the de-excitation of the activated material which are measured when the detectors are turned on again. As the high count rates after the SAA originate from nuclear de-excitation, its influence should decay exponentially over time and should have the functional form

$$R_{\text{SAA}}(t) = R_{\text{SAA}}(t_0) \cdot \exp(-C_{\text{decay}} \cdot (t - t_0)). \quad (4)$$

Because of the different elements in the satellite's and the detector's material, there should be a superposition of several exponential decays after each SAA exit. In order to keep the computational effort manageable, we included only two decay functions after each exit to allow for a fast and a slow decay. The fast decaying part usually decays in \approx minutes, and is thus completely gone before the next SAA passage. But the slowly decaying part can take several hours to decay completely which causes accumulation of background signal by consecutive SAA passages. This activation decays slowly during the long time of the day with no SAA passage. This leads to four parameters per SAA exit, one for each decay constant and the two corresponding normalizations. It is clearly visible in Fig. 7 that the model is able to explain the rapidly decaying count rates after the SAA passage, and is significantly reducing the peaks in the residuals.

The presented procedure for the SAA influence depends on the boundaries, which are used by the Fermi team, being correct. If the boundaries of the SAA are wrong it can happen, that the detectors are for example turned off a bit too late, which leads to a rise in the count rates before the official SAA entrance.

As the SAA shape and dimension changes due to solar activ-

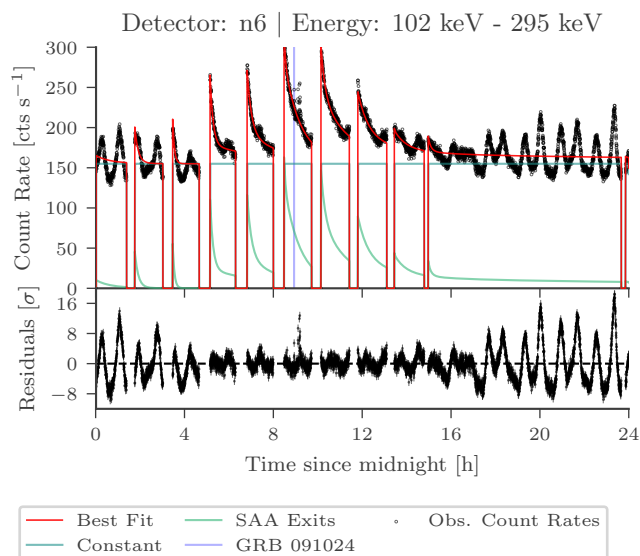


Fig. 7: Same as Fig. 6, but including the additional SAA component. The peaks in the residuals after the SAA exit have disappeared. The GBM trigger time for GRB 091024 is marked by a cyan line.

ity, and is also slowly moving over the years, the Fermi team is adapting the SAA boundaries as needed, so that such outliers should be very small in number. To be on the safe side one could always ignore some time (few hundreds of seconds) before and after the official SAA transition.

3.3.3. Earth Albedo

The Earth is known to be a source of γ -rays in the GBM energy range (Thompson et al. 1981; Ajello et al. 2008). These γ -rays are produced by cosmic rays colliding with molecules in the Earth’s atmosphere through π^0 -decay and bremsstrahlung (Petty 2005; Abdo et al. 2009). The spectrum of the produced γ -rays that are emitted back into space is called ‘Earth Albedo’ and is shown in Fig. 8 in comparison to the Cosmic Gamma-Ray spectrum.

The secondary particles produced in the collision of a cosmic ray with an atmospheric molecule tend to fly in the same direction as the primary cosmic ray because of momentum conservation. As cosmic rays mostly consist of protons, they get deflected eastwards upon impinging Earth’s magnetic field, therefore the cosmic ray flux from the west as seen by the satellite is larger. It has been shown by Petty (2005) that the East-West asymmetry in the Earth Albedo peaks at a photon energy in the GeV range and is small at lower energies in the MeV range. Abdo et al. (2009) showed that the effect is also very small for very high energies (\approx TeV). Additionally, nearly the whole photon flux with very high energies (\approx TeV) originates from a small ring around the Earth (as seen by the satellite). This ‘ring effect’ weakens towards lower γ -ray energies, therefore we assume that in the keV to low MeV region this effect can be neglected (Abdo et al. 2009).

It is therefore reasonable to assume that the East-West and the ring effect, that are well observed at higher energies, is not significant in the keV to low MeV energy region and therefore to assume that the Earth Albedo at these energies is isotropic over the whole Earth surface seen by the satellite.

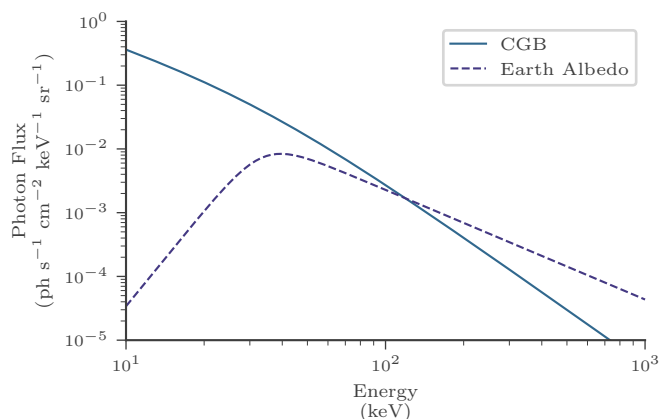


Fig. 8: The spectra of the Cosmic Gamma-Ray Background (CGB) and the Earth Albedo for spectral parameters given in (Ajello et al. 2008). The spectrum of the CGB is higher than the one of the Earth Albedo for energies smaller than \approx 120 keV, but for higher energies the spectrum of the CGB has a steeper slope which causes that the Earth Albedo to surpass the CGB spectrum for energies higher than \approx 120 keV.

The variation of the background from the Earth Albedo in the individual detectors is caused by the different positions of the Earth in the satellite coordinate system for different times and the therefore changing effective response (see Sec. 3.2). Fig. 9 shows the model expanded by the component for the Earth Albedo. The assumed functional form of the Earth Albedo spectrum in this paper is a smoothly connected double power law with the spectral parameter values as given in Ajello et al. (2008), but we free the normalization C and fit it to the GBM data (see Eq. 5).

$$\frac{dN}{dE} = \frac{C}{\left(\frac{E}{33.7\text{keV}}\right)^{-5} + \left(\frac{E}{33.7\text{keV}}\right)^{1.72}} \quad (5)$$

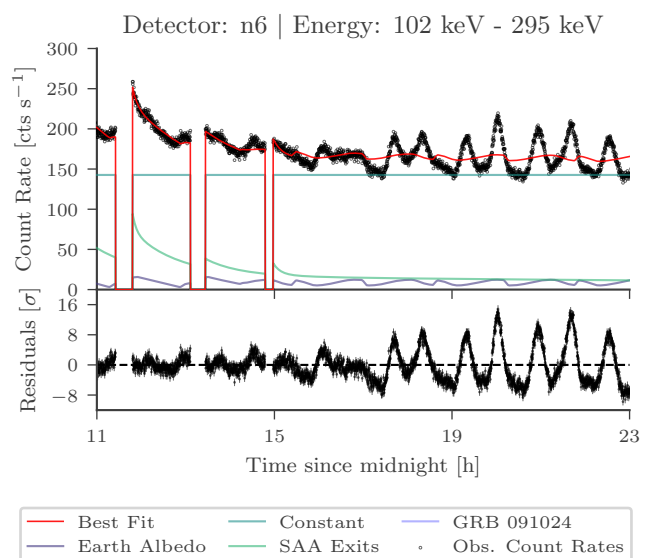


Fig. 9: Same as Fig. 7 but only for half of the day for better legibility and including the Earth Albedo as additional background source.

3.3.4. Cosmic Gamma-Ray Background

The Cosmic Gamma-Ray Background (CGB), which was discovered more than 50 years ago, is generally agreed to be produced by emission of unresolved extra-galactic point sources (Giacconi et al. 1962; Hasinger 2004; Ajello et al. 2008). The galactic contribution to the CGB is subdominant for photon energies below 1 MeV. (Bouchet et al. 2011; Ajello et al. 2008) and almost the entire Cosmic X-ray background (CXB) for energies smaller than 2 keV is accounted for by Active Galactic Nuclei (AGN) that host accreting super-massive black holes (Hasinger 2004). For energies above 6 keV on the other hand, the fraction of CGB emission that can be resolved into AGN is smaller than 50% (Worsley et al. 2005). This unresolved CGB flux could be explained by photon emission of a yet undetected population of highly absorbed AGN. The spectrum of the CGB is shown in Fig. 8 for the spectral parameters given in Ajello et al. (2008).

Fig. 10 shows the model expanded by the component for the CGB. The assumed functional form of the CGB spectrum in this paper is a smoothly connected double power law with the spectral parameter values as given in Ajello et al. (2008), but we free the normalization C and fit it to the data (see Eq. 6). It was additionally shown theoretically by Churazov et al. (2008) that a significant percentage of the CGB spectrum in the keV range gets reflected by the Earth. As this is a second order influence it is currently not included in the work, but we plan to include this reflection of the CGB from the Earth in the future.

$$\frac{dN}{dE} = \frac{C}{\left(\frac{E}{30\text{keV}}\right)^{1.32} + \left(\frac{E}{30\text{keV}}\right)^{2.88}} \quad (6)$$

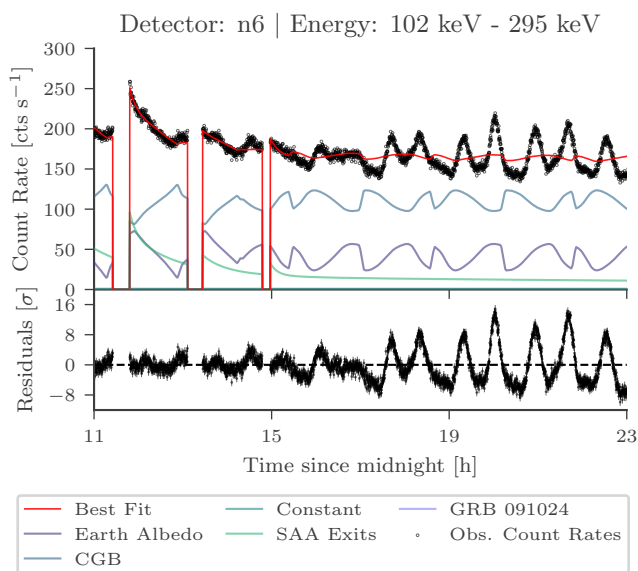


Fig. 10: Same as Fig. 9 but including the Cosmic Gamma-Ray Background as additional background source. The influence of the Earth Albedo and the CGB are strongly correlated. When the influence of the Earth Albedo is high the Earth is covering a part of the response with high effective area and also blocks the CGB photons from this direction and therefore leads to a lower influence of the CGB.

3.3.5. Cosmic Rays

Cosmic rays that hit the satellite can either leave a direct signal in the detectors, that is converted into a certain PHA channel, or excite atoms in the satellite material that upon de-excitation produce photons (as shown for INTEGRAL/SPI in Diehl et al. (2018)) which can be measured by GBM's detectors. Due to Fermi's low-Earth orbit and the small inclination, the detectors are well protected by the Earth magnetic field against cosmic rays. Only the cosmic rays with very high energies ($> \text{GeV}$ for protons) can reach the satellite (Pesce-Rollins 2009). This shielding of cosmic rays varies during the orbital motion with the different magnetic field strength of the Earth in different orbital positions and therefore the amount and the spectrum of cosmic rays hitting the satellite is time dependent. We will introduce two different approaches to model the cosmic ray contribution, first by using the McIlwain L-parameter and second by the use of the data in the high-energy BGO channels.

The McIlwain L-parameter (McIlwain 1966) can be used as quantifier to model this shielding effect against cosmic rays by the Earth's magnetic field as has been shown for example for protons and electrons measured by the LAT in Pesce-Rollins (2009). The McIlwain L-parameter is connected to the magnetic cutoff rigidity R_C as given in Eq. 7. The parameters K and α change with time and have to be determined for the corresponding time (Shea et al. 1987).

$$R_C = KL^{-\alpha} \quad (7)$$

If one extends the magnetic field line at a position to the magnetic equator, then the L-parameter at that position gives the distance of the magnetic field line at the magnetic equator to the Earth center in units of Earth radii. The correct functional dependence of the background rate caused by cosmic rays on the L-parameter is not known. All that is known a priori is that a higher L-parameter means a weaker protection by the Earth magnetic field and thus should lead to a higher background caused by cosmic rays. During our work we found that assuming a linear relationship between the background rate difference and the L-parameter difference seems to describe the detected background rates quite well for the GBM detectors and the L-parameter range on the Fermi orbit (≈ 1 -1.7 outside of the SAA as shown in Pesce-Rollins (2009)).

$$R(L_1) - R(L_2) \propto L_1 - L_2 \quad (8)$$

For cosmic rays it is assumed that Eq. 8 describes the difference in the count rates for different L-parameter values. To get the McIlwain L-parameter values for the different times the weekly spacecraft file² is used. Parameter values are provided with a time resolution of 30s. Between these time steps a linear interpolation is used. Due to the fact that we only have a formula for the difference in the rate for different L-parameters, the total rate due to the cosmic rays is defined as

$$R_{CR} = R_{CR}(L_{min}) + C_{McIlwain} \cdot (L - L_{min}). \quad (9)$$

Here L_{min} is the minimal L-parameter of the data. Therefore, the background model component has two parameters: Firstly, a constant $R_{CR}(L_{min})$, which is the same for all time bins, and secondly, a normalization $C_{McIlwain}$, which is multiplied by the difference of the L-parameter of the time bin and the minimal L-Parameter in the data. This constant contribution motivates

² from heasarc.gsfc.nasa.gov/FTP/fermi/data/lat/weekly/spacecraft/

the use of our constant source we introduced in Sect. 3.3.1. The influence of the cosmic rays in our model is direction independent. This seems to be true to first order, but we see in the high-energy channels, where the cosmic ray contribution is dominant, directional differences of a few tens of percent that can not be explained by our model. This could be explained by the East-West asymmetry of the cosmic ray flux due to the Earth magnetic field (see Sec. 3.3.3).

Because the influence of cosmic rays on GBMs background is rising with energy, one can assume that in the high-energy channels of the BGO detectors the background is strongly dominated by cosmic rays. This can be used as an alternative to model the cosmic ray contribution. To obtain the functional form, we binned the BGO data in the energy range of 8.6 MeV to 16.6 MeV to 100s and fit a spline of 3rd degree with a smoothing prior. It is then assumed that the variation in the amount of background rates caused by cosmic rays in the lower energies is linearly correlated with the functional obtained from the BGO data; therefore, we only fit for the normalization $C_{\text{BGO-Approx}}$ that is multiplied with the fitted spline S_{BGO} .

$$R_{\text{CR}} = C_{\text{BGO-Approx}} \cdot S_{\text{BGO}} \quad (10)$$

The model obtained by the BGO approximation (Fig. 12) can fit the cosmic ray contribution noticeably better than the model that uses the McIlwain L-parameter (Fig. 11). But of course one has to keep in mind that the BGO data is not free of other background sources as for example the spectrum of the Earth Albedo, that was introduced in Sec. 3.3.3, extends to the MeV range. This shortfall could be overcome by the use of the Anti-Coincidence Detector (ACD) of the LAT to model the cosmic ray background in GBM. The ACD is primarily used to detect charged particles in 89 tiles around the LAT, in order to exclude the charged particle induced background in the LAT data. Because the count rates of the ACD are also stored, one could use the different tiles to reconstruct the particle flux variation for different sites of the satellite individually. Unfortunately, the data of ACD is not publicly available, which is why we leave this approach for future improvements of the model and use the BGO approximation in the following sections.

The BGO approximation is the only empirical model component in this paper. This is due to the complex processes that lead to the background contribution by the cosmic rays, like their deflection in the earth magnetic field and how they activate the satellite material. An appropriate procedure to deal with this would be a full simulation, but unfortunately there is no public mass model of the Fermi satellite that could be used to setup such a simulation.

3.3.6. Point Sources

The CGB is not completely homogeneous due to a plethora of resolved point like sources. Additionally there are very bright galactic point sources like the Crab nebula. Their influence is more significant in the lower energy channels up to 100 keV as most sources are thermal, with a spectrum rapidly falling with increasing energy. These point sources can be seen in the background of the detectors of GBM as shown in Fig. 13. To reduce the computational time we only take one point source into account, namely the Crab, but we plan to add more point sources in the future. The spectrum of the Crab as described in Madsen

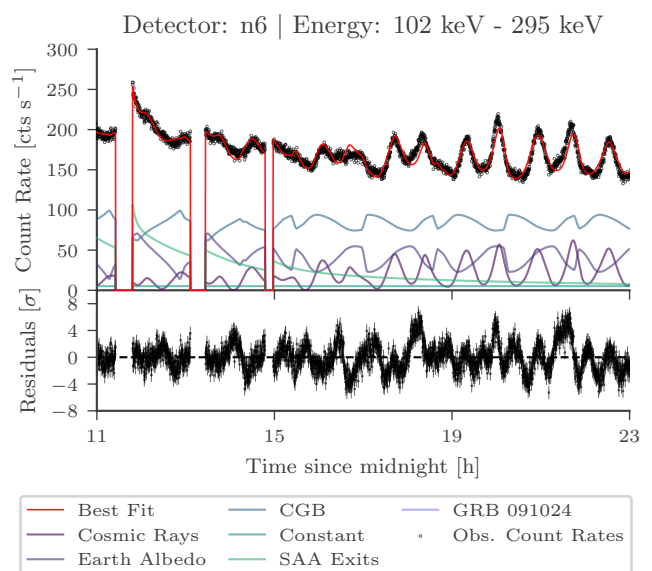


Fig. 11: Same as Fig. 10, but including the cosmic ray component. For this plot the McIlwain L-parameter model is used. It is clearly visible that the fast raising and lowering of the count rates is mainly caused by the difference of cosmic rays reaching the detector.

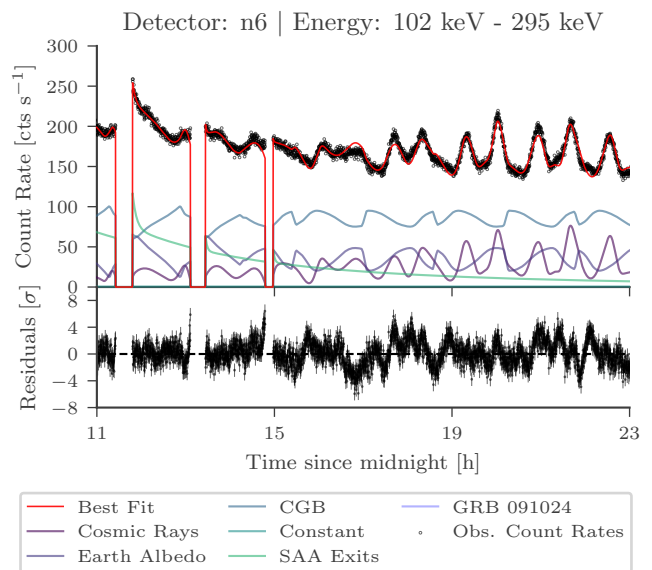


Fig. 12: Same as Fig. 10, but including the cosmic ray component. For this plot the BGO approximation model is used. It is clearly visible that the fast raising and lowering of the count rates is mainly caused by the difference of cosmic rays reaching the detector. The BGO approximation can fit the data noticeably better than the McIlwain L-parameter model (see Fig. 11).

et al. (2017) is used (see Eq. 11) and we again fit the normalization C to the data.

$$\frac{dN}{dE} = \frac{C}{E^{2.1}} \quad (11)$$

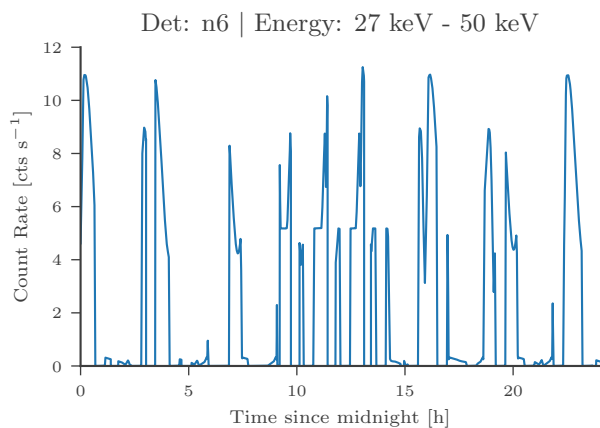


Fig. 13: The expected temporal count rate variation for the reconstructed energy range 27 to 50 keV caused by the Crab Nebula with a spectrum as given in Eq. 11 with $C=9.7$ (Madsen et al. 2017).

3.3.7. Sun

The Sun can be treated as a special point-like source, which also emits X-rays in the low keV range. The spectrum was investigated in Hannah et al. (2007), where 2σ upper limits are given for the photon flux of the quiet Sun from 3 keV to 200 keV. Even if these upper limits would be the actual spectrum of the Sun, the influence of the Sun would be very small and, if at all, only visible in the lowest detector channels of GBM.

An exception are the eruptions of the Sun, when it violently releases a large amount of particles and photons with higher energies. While the particles of these so-called solar flares are deflected by the Geomagnetic field, the photons reach GBM and are clearly visible in the data. Information about the flares can be obtained from the yearly flare files which are produced by the National Center for Environmental Information (NOAA). The solar flares can be modeled by an exponential decay function, which is set to zero up to the time when the flare arrives. To keep the number of parameters manageable we do not include solar flares in the model at the moment. If there is a strong solar flare we simply exclude this time interval from the analysis. The quiet Sun is modeled as a simple power law spectrum in the following.

3.4. Fitting

The resulting background model has a total of 50 free parameters for one day, one reconstructed energy channel and one detector, including the following:

- Two normalization and two decay constants for every SAA exit (≈ 40 parameters in total; depends on the number of SAA exits during the day).
- Two normalization and two decay constants for leftover excitation at the beginning of the day (4 parameters).
- Normalization for Earth Albedo, Cosmic Gamma-ray Background, Sun, point sources (only Crab at the moment), cosmic ray contribution (5 parameter).
- One constant

We fitted the free parameters of our model to the data using the Bayesian nested sampler MultiNest (Feroz et al. 2009; Buchner

et al. 2014).

As our model should represent the total count rates of GBM, we do not have a ‘background’ signal. Thus, the correct likelihood is a Poisson likelihood without background, namely the one given in Cash (1979):

$$\log(\mathcal{L}) = \sum_{\text{time bins}} \left[N_{\text{model}}(t) - N_{\text{data}}(t) \cdot \log(N_{\text{model}}(t)) \right] \quad (12)$$

The parameter estimation of our model with the data of one day and one reconstructed energy channel takes $\approx 1:30\text{h}$ with 32 cores (Intel(R) Xeon(R) Platinum 8168 CPU @ 2.70GHz) producing full posterior distributions. A Bayesian way of checking the model’s ability to describe the observed data are posterior predictive checks (PPC) (Gabry et al. 2017; Burgess et al. 2019). By the use of the posterior predictive distribution

$$\pi(y^{\text{sim}}|y^{\text{obs}}) = \int \pi(y^{\text{sim}}|\theta)\pi(\theta|y^{\text{obs}})d\theta \quad (13)$$

where $\pi(\theta|y^{\text{obs}})$ is the posterior distribution of θ and $\pi(y^{\text{sim}}|\theta)$ the probability of a new simulated observation given a set of parameters θ , one can generate simulated data and compare it to the original observed data. We sampled 300 parameter sets from the posterior distribution and simulated new data for each of these sets using the underlying Poisson distribution of photon counts. The observed data should be similar to the simulated data which can visually be checked by making the area which contains 95% of the simulated data and verifying if the observed data lies within. It is a strong indication that the fit is wrong if many observed data points lie outside of this marked area. This area that contains 95% of the simulated data is marked as green area around the best fit in the following.

The shown Poisson residuals are computed under the hypothesis that there is no uncertainty in the background. In other words, the probability of obtaining the observed counts is computed, given the expected counts from the background and then transforming it in units of sigma.

4. Results

To demonstrate the usefulness of our newly developed background model in a practical setting we now provide several fits of the model to different days. In 4.1 we show how the model can be used to fit the background for the GRB 110920A for which the classical approach of using polynomial fits can give ambiguous answers. After this we show in 4.2 that the multiple emission peaks over more than 1000 seconds caused by the ultra long GRB 091024 does not effect our fit even if we do not exclude the emission times from the fit. To check this for an even more extreme case we show in 4.3 the background fit for the 21st June 2015, which was during the time of a V404 Cygni outburst. This outburst caused several very long emission periods seen in GBM during this day. We will show that even such an extreme event only slightly disturbs our background fit and that we can identify more emission times than the ones that triggered GBM. In the final example we show that we can identify untriggered excess emission for GRB 130925A with this background model.

4.1. GRB 110920A

GRB 110920A was a bright, single pulse GRB that occurred only about 100 seconds after an SAA exit of GBM. This causes the background to have a significant component from the exponential decay of the activated material. In Fig. 14 we show that our model can explain the background around GRB 110920A very well. For an accurate fit of the background during the source time of the GRB event we had to exclude the time of the GRB event from the fit, because it happened so shortly after an SAA exit, that it disturbed the SAA exit fit badly. But we see the GRB as clear deviation from the background fits even without excluding the time, which means that this GRB could have been found with the background model without prior knowledge of the time of the GRB event.

In Fig. 15 we show the problems that can occur when one is using the classical polynomial approach for a background that can not really be fitted by a polynomial, as it contains a significant component from the exponential decay of the activated material after the SAA exit. The figure shows different polynomial fits, for different background time selections around the GRB event. One can see, that the background fits are quite different during the active time of the GRB but all look equally valid in a short time around the GRB event (± 50 seconds). This random choice of one of these background polynomials can be overcome with our background model, that gives only one unambiguous answer.

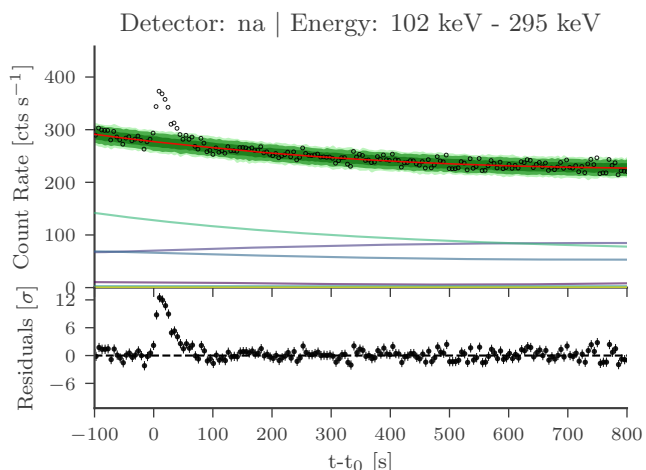


Fig. 14: Background fit for the time around GRB 110920A in the reconstructed energy range of 102 to 295 keV for detector na with a time-bin size of 5 seconds. The model can fit the background very well and the GRB is well visible in the residuals.

4.2. Ultra-Long GRB 091024

In this subsection we present the background fits for the 24th October 2009, that contains the previously reported ultra-long GRB 091024 (Gruber et al. 2011). GRB 091024 was detected by Fermi-GBM (Bissaldi & Connaughton 2009), Swift-BAT (Marshall et al. 2009) and Konus-Wind (Golenetskii et al. 2009) and consisted of multiple emission peaks with a total duration of about 1000 seconds. The last emission peak had a duration of about 230 seconds, which makes it an ideal test case, to evaluate if this long, multiple emission period could have effected our

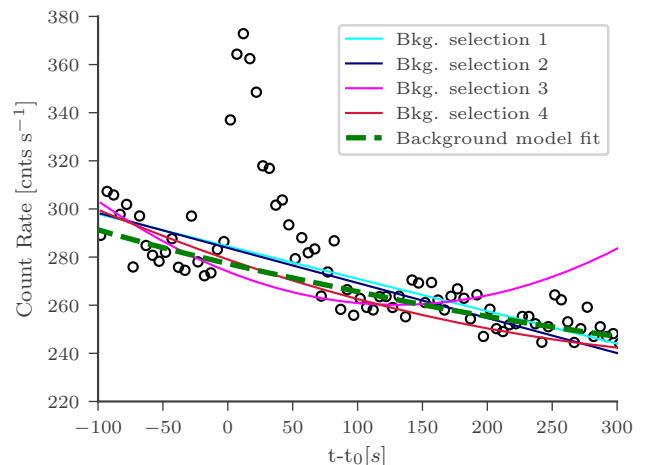


Fig. 15: Data and different background estimations for the time around GRB 110920A in the reconstructed energy range from 102 to 295 keV for detector na with a time-bin size of 5 seconds. The four solid lines are derived with the classical approach of fitting polynomials to the time before after the transient event, each with a different definition of these times (1: -100s to -90s and 150s to 200s; 2: -100s to -70s and 50s to 200s; 3: -100s to 0s and 100s to 200s; 4: -100s to -50s and 400s to 500s). Additionally the best fit of our background model is plotted as dashed green line. It is clear that the 4 different polynomial background estimation give different results, that all look equally valid in a short time around the GRB event (± 50 seconds), which makes a random choice of one of them necessary, whereas the fitted background model gives an unambiguous answer.

background fit.

Fig. 16 and 17 show the data (black) and the best fit of the total background model (red) for the two reconstructed energy ranges 27–50 keV and 102–295 keV for detector n8. The lower energy range is, as previously discussed, dominated by the Cosmic Gamma-ray Background and the Earth Albedo, while the cosmic ray component is negligible. In the reconstructed energy range from 102–295 keV the cosmic ray component is already important.

It is clearly visible in the residuals and with the posterior predictive check, that the model can explain most of the observed data very well. In both reconstructed energy ranges an excess of count rate for the trigger time is already visible in Fig. 16 and 17, but is much more obvious in Fig. 18, which shows the background fit for three different detectors and two different reconstructed energy ranges around the trigger time of GRB 091024. Here, the multiple emission peaks are clearly visible as deviations from the background fit, demonstrating the usefulness of a physically motivated background model to identify long-duration emission, and the possibility to use the fitted background model as background estimation during the active time of the transient source.

We can also see a second strong deviation from the fitted background model in the low energy range at about 21 hours after midnight, for which we checked that it is not from the same location as GRB 091024. This could be due to a soft transient source.

Additionally, there are two long-duration, significant (up to 10

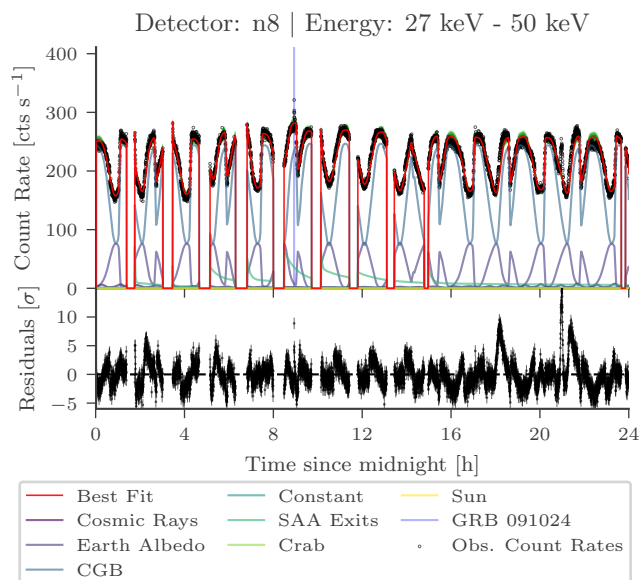


Fig. 16: Data and background fit for 24/10/2009 including the ultra-long GRB 091024 for detector n8 in the reconstructed energy range of 27–50 keV with a time-bin size of 15 s. In the low energy range the background is dominated by the CGB, but also has some significant contribution from the Earth Albedo and the SAA exits. The plot shows the influence of the different sources in different colors, the best fit total model in red and the detected count rates in black. The GBM trigger time of GRB 091024 is marked by a cyan line.

sigma) deviations from the fitted background model in the reconstructed energy range 27–50 keV. This could be due to a missing point source in our model, as we see this deviation in three detectors, that point in a similar direction (n6, n7 and n8), at similar (but not equal) times. To remove such deviations, we plan to include more known point sources in the background model in the future.

4.3. V404 Cygni flaring

In June 2015 V404 Cygni went into outburst, producing multiple flares which GBM triggered on (Jenke et al. 2016).

The 21st of June was a very active day, on which GBM triggered 10 times. We present the light curves of GBM for two energy channels and three detectors for part of the day in Fig. 19. We have marked the times of all GBM triggers with blue vertical lines. One can clearly see from the PPCs and the residuals that there were several more long and weak emission periods on this day, that did not trigger GBM. We marked some of these times roughly with red vertical lines in the plots. While we have not determined the sky positions of all these additional emission events, the similarity in the gamma-ray spectrum to that of the triggered events makes the V404 Cyg origin very likely. V404 Cyg was so active on that day that it disturbed the background fit a bit, as the background fit is slightly too high for the non-active times of V404 Cygni. But still the several emission periods are well visible in the plots even though we did not exclude the times when V404 Cygni was active from the fit. This is due to the fact that we use physical derived background sources and not arbitrary polynomials and therefore very strongly restrict what kind of shapes can be fitted by our background model.

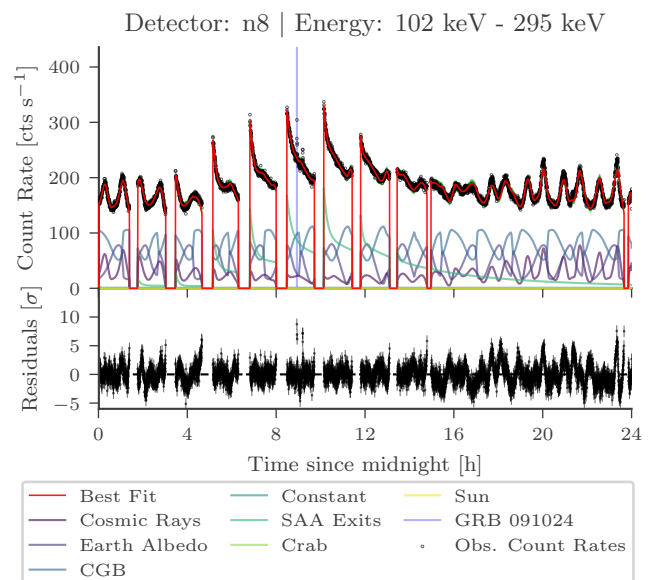


Fig. 17: Data and background fit for 24/10/2009 including the ultra-long GRB 091024 for detector n8 in the reconstructed energy range of 102–295 keV with a time-bin size of 15 s. In this reconstructed energy range the contribution from the cosmic rays is also important. The GBM trigger time of GRB 091024 is marked by a cyan line.

This makes the presented background model a promising tool to search for long source emissions in the data of GBM in the future.

If one wants to use the fitted background model as an accurate background estimation during the active times of the source, one should of course redo the analysis and exclude the times when the source was active from the fit, to get rid of this disturbance.

4.4. Identifying untriggered excess emission

Since our background model is fit over a full day, the fit parameters have no room to allow variations between individual satellite orbits, i.e. to accommodate spatially (e.g. transient sources) or temporally (e.g. disturbances in the magnetic field) varying sources. This makes the background fit very stiff, and thus allows us to readily identify variable sources. This is demonstrated for September 25, 2013, when multiple emission periods were detected over several thousand seconds from the ultra-long GRB 130925A (e.g. Golenetskii et al. 2013). In Fig. 20 the data for detector n9 and four reconstructed energy ranges are displayed, as well as our fitted model (red). The two GBM triggers are marked as vertical lines. The other emission period(s), nicely covered by Konus-Wind, verify the identification of late GRB 130925A emission with GBM.

4.5. Comparison to “Fermi GBM Orbital Background Subtraction Tool”

The advantage of the presented background model with respect to the “Fermi GBM Orbital Background Subtraction Tool”³

³ https://fermi.gsfc.nasa.gov/ssc/data/analysis/user/osv_1.3.tar

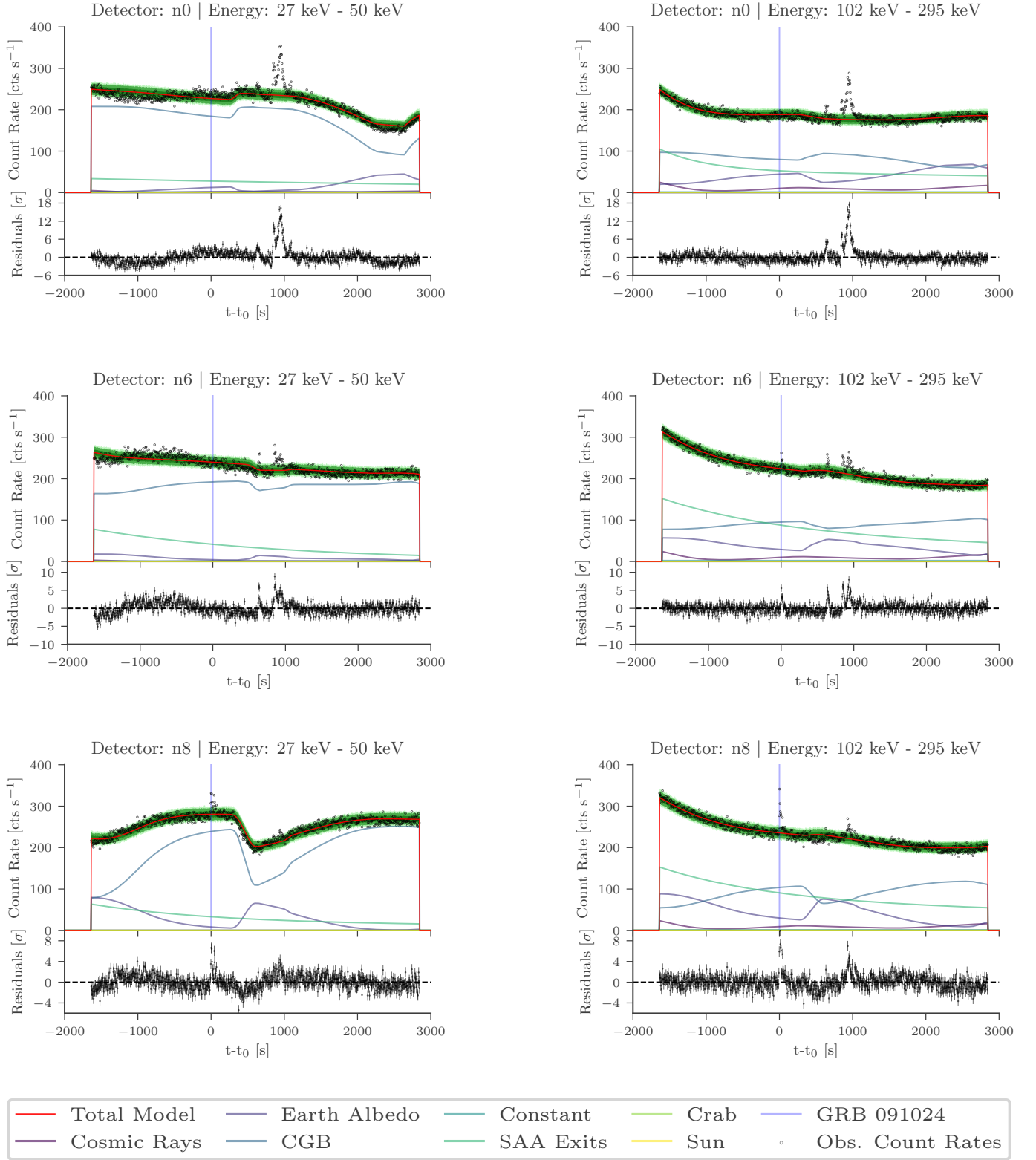


Fig. 18: Data and background fits for the 5000 seconds around the GBM trigger time of GRB 091024 for three different detectors (n0 (top), n6 (middle), n8 (bottom)) and two reconstructed energy ranges (27-50 keV (left) and 102-295 keV (right)). The multiple peak emission with a total duration of more than 1000 seconds after the GBM trigger ($t=0$) are clearly visible as deviations from the background fit. Due to the long duration of GRB 091024 the detector with the smallest offset angle to the GRB position has changed from the first to the last peak from n8 to n0, which explains why the last peak is clearly visible in the light curves of n0 while the first peak is not.

(OSV) (Fitzpatrick et al. 2012) is also demonstrated for September 25, 2013 (Fig. 20), where the estimation of the OSV is overplotted in dark blue. One can see that our model is capable of explaining the background variations in all four reconstructed energy ranges, whereas the OSV fails, mainly due to an Autonomous Repoint Request (ARR) after the second GBM trigger. But also during days without ARR, the OSV method has its limitations (Fig. 21 and 22), as it depends on having no deviation of any kind (besides ARR also transients etc) also 30 orbits before and after the day in question. With about 1 onboard trigger every 10 orbits (<https://gammaray.nsstc.nasa.gov/gbm/>), this limitation affects the background estimation for some period of time on $\sim 30\%$ of all days.

The following summarizes the advantages of our physical model:

- is not affected by ARR or other deviations from the normal pointing mode,
- is not affected if the satellite was in an SAA 30 orbits before or after the time of interest,
- is not affected by GRBs or any transient sources occurring 30 orbits before or after the time of interest,
- is a more robust method that does, for example, not need the radiation environment or magnetic field to be stable for at least 3 days (due to the ± 30 orbits that are used in the OSV),
- treats the data in a statistically correct way which allows to derive proper errors on the background counts,
- allows us to understand and study the different components of the background (also interesting for future missions).

5. Conclusion

The derivation of a physically motivated background model for GBM was presented. It consists of six different source components (Earth Albedo, Cosmic Gamma-ray background, Sun, point sources (just the Crab at the moment), South Atlantic Anomaly and cosmic rays), where only the cosmic-ray contribution is modeled empirically.

The presented model is capable of modeling the background for most of the GBM PHA channels as shown for the example cases of the ultra-long GRB 091024, the V404 Cygni outburst in June 2015 and GRB 110920A.

There are three obvious possible future applications of this physically motivated background model:

1. Use it as a new approach to search for ultra-long GRBs in the 12+ years of GBM data, that until now have been indistinguishable from the background variations.
2. Infer information about the different background components, for example the Cosmic Gamma-ray Background spectrum in the GBM energy range.
3. Develop a transient search algorithm for slowly rising or long transients which are not recognized by the onboard trigger algorithm.

References

Abdo, A. A., Ackermann, M., Ajello, M., et al. 2009, *Phys. Rev. D*, 80, 122004
 Ajello, M. et al. 2008, *Astrophys. J.*, 689, 666
 Berlato, F., Greiner, J., & Burgess, J. M. 2019, *ApJ*, 873, 60
 Bissaldi, E. & Connaughton, V. 2009, *GCN Circular* 10070
 Bissaldi, E., von Kienlin, A., Lichti, G., et al. 2009, *Experimental Astronomy*, 24, 47

Bouchet, L., Strong, A. W., Porter, T. A., et al. 2011, *The Astrophysical Journal*, 739, 29
 Buchner, J., Georgakakis, A., Nandra, K., et al. 2014, *A&A*, 564, A125
 Burgess, J. M. 2019, *GBM DRM Generator*
 Burgess, J. M., Greiner, J., Bégué, D., & Berlato, F. 2019, *MNRAS*, 490, 927
 Burgess, J. M., Yu, H.-F., Greiner, J., & Mortlock, D. J. 2018, *MNRAS*, 476, 1427
 Cash, W. 1979, *ApJ*, 228, 939
 Churazov, E., Sazonov, S., Sunyaev, R., & Revnivtsev, M. 2008, *Monthly Notices of the Royal Astronomical Society*, 385
 da Silva, M. R. & Rocco, E. M. 2017, *Journal of Physics: Conference Series*, 911, 012005
 Diehl, R., Siebert, T., Greiner, J., et al. 2018, *A&A*, 611, A12
 Feroz, F., Hobson, M. P., & Bridges, M. 2009, *MNRAS*, 398, 1601
 Fitzpatrick, G., McBreen, S., Connaughton, V., Briggs, M., & Team, t. G. 2012, *Proc SPIE*, 84433B
 Gabry, J., Simpson, D., Veltari, A., Betancourt, M., & Gelman, A. 2017, *arXiv e-prints*, arXiv:1709.01449
 Ganushkina, N. Y., Dandouras, I., Shprits, Y. Y., & Cao, J. 2011, *Journal of Geophysical Research (Space Physics)*, 116, A09234
 Giacconi, R., Gursky, H., Paolini, F. R., & Rossi, B. B. 1962, *Phys. Rev. Lett.*, 9, 439
 Golenetskii, S., Aptekar, R., Frederiks, D., et al. 2013, *GCN Circular* 15260
 Golenetskii, S., Aptekar, R., Mazets, E., Pal'shin, V., & Frederiks, D. 2009, *GCN Circular* 10083
 Greiner, J., Burgess, J. M., Savchenko, V., & Yu, H.-F. 2016, *The Astrophysical Journal*, 827, L38
 Gruber, D., Krühler, T., Foley, S., et al. 2011, *A&A*, 528, A15
 Hannah, I. G., Hurford, G. J., Hudson, H. S., Lin, R. P., & van Bibber, K. 2007, *ApJ*, 659, L77
 Hasinger, G. 2004, *Nuclear Physics B Proceedings Supplements*, 132, 86
 Hoover, A. S., Kippen, R. M., Meegan, C. A., et al. 2005, *Nuovo Cimento C Geophysics Space Physics C*, 28, 797
 Horiuchi, S., Ng, K. C. Y., Gaskins, J. M., Smith, M., & Preece, R. 2015, *arXiv e-prints*, arXiv:1502.03399
 Jenke, P. A., Wilson-Hodge, C. A., Homan, J., et al. 2016, *The Astrophysical Journal*, 826, 37
 Kippen, R., S. Hoover, A., Wallace, M., et al. 2007, *AIP Conference Proceedings*, 921
 Madsen, K. K., Forster, K., Grefenstette, B. W., Harrison, F. A., & Stern, D. 2017, *Astrophys. J.*, 841, 56
 Marshall, F., Baumgartner, W., Beardmore, A., et al. 2009, *GCN Circular* 10062
 McIlwain, C. E. 1966, in *Radiation Trapped in the Earth's Magnetic Field*, ed. B. M. McCormac (Dordrecht: Springer Netherlands), 45–61
 Meegan, C., Lichti, G., Bhat, P. N., et al. 2009, *ApJ*, 702, 791
 Mozzoni, D. T. 2007, PhD thesis, The Florida State University
 Pendleton, G. N., Briggs, M. S., Kippen, R. M., et al. 1999, *ApJ*, 512, 362
 Pesce-Rollins, M. 2009, *arXiv e-prints*, arXiv:0912.3611
 Petry, D. 2005, *AIP Conf. Proc.*, 745, 709
 Schaefer, R. K., Paxton, L. J., Selby, C., et al. 2016, *Space Weather*, 14, 330
 Shea, M. A., Smart, D. F., & Gentile, L. C. 1987, *Physics of the Earth and Planetary Interiors*, 48, 200
 Szécsi, D., Bagoly, Z., Kóbori, J., Horváth, I., & Balázs, L. G. 2013, *A&A*, 557, A8
 Thompson, D. J., Simpson, G. A., & Ozel, M. E. 1981, *J. Geophys. Res.*, 86, 1265
 van Allen, J. A. & Frank, L. A. 1959, *Nature*, 183, 430
 Worsley, M. A., Fabian, A. C., Bauer, F. E., et al. 2005, *MNRAS*, 357, 1281

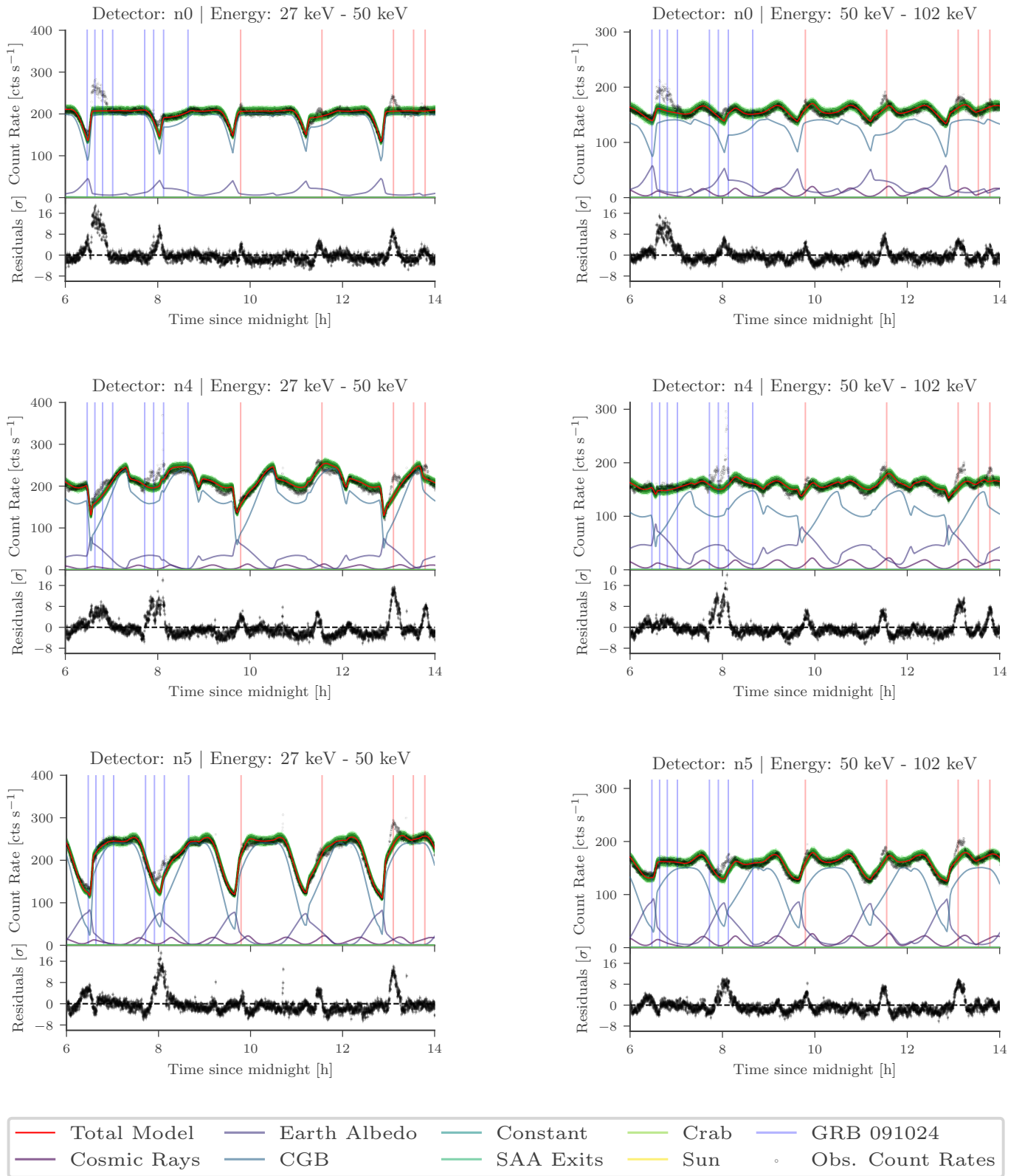


Fig. 19: Data and background fits for part of the 21st June 2015 that was during a V404 Cygni outburst for three different detectors (n0 (top), n4 (middle), n5 (bottom)) and two reconstructed energy ranges (27–50 keV (left) and 50–102 keV (right)). It is clearly visible that there are many emission periods during the day that stick out of our background model fit. The blue vertical lines are GBM trigger times, whereas the red vertical lines are possible new emission events that did not trigger GBM.

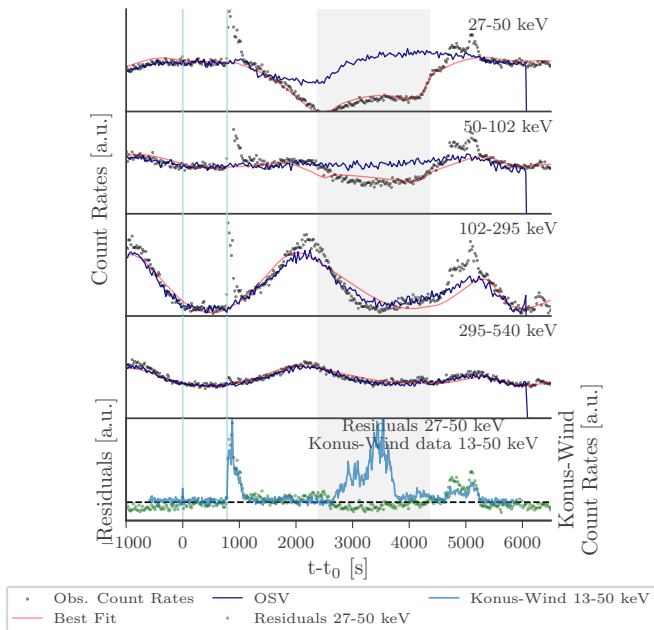


Fig. 20: Data (black), background fit (red) and background estimation (OSV, dark blue) with the “Fermi GBM Orbital Background Subtraction Tool” (Fitzpatrick et al. 2012) for the emission time of 130925A, detector n9 and four reconstructed energy ranges in the top four panels. In the lower panel the residuals for the background fit between 27 and 50 keV reconstructed energy are given, as well as the background subtracted Konus-Wind data between 13 and 50 keV (Golenetskii et al. 2013). The two blue vertical lines show the time of the two GBM triggers for GRB 130925A and the grey area the time during which the position of GRB 130925A was occulted by the earth for GBM. The un-triggered excess emission at ≈ 5000 seconds after the first GBM trigger is clearly visible in the displayed residuals of the background fit, and fit temporally nicely to the data of Konus-Wind.

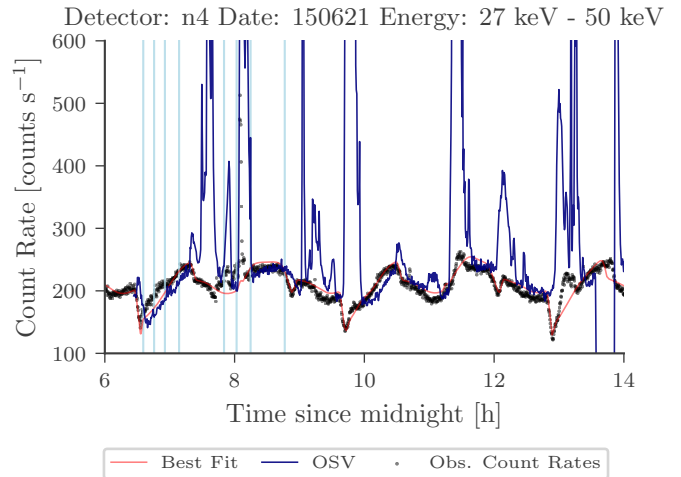


Fig. 21: Data (black), background fit (red) and background estimation (OSV, dark blue) with the “Fermi GBM Orbital Background Subtraction Tool” for part of 21st June 2015 during the 2015 V404 Cygni outburst, detector n9 and reconstructed energy between 27 and 50 keV. One can see that the OSV estimation fails badly due to the many strong and long emission periods that V404 Cygni produced 30 orbits before and after the shown time, whereas our model fits can explain the background well. All GBM triggers during this time are shown as blue vertical lines (before the onboard triggers were turned off).

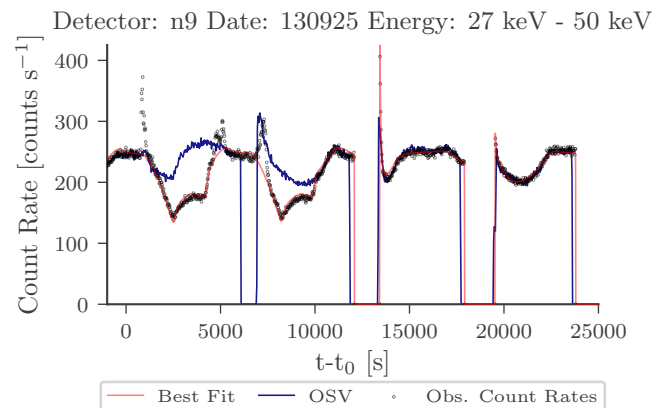


Fig. 22: Data (black), background fit (red) and background estimation (OSV, dark blue) with the “Fermi GBM Orbital Background Subtraction Tool” for 25000 seconds on the 25th September 2013. One can see that the OSV estimation fails during the first 10000 seconds due to an ARR but gets better after the satellite returned to normal pointing mode. But it does not get better than our model, which can fit all the data well. And for about 1000 seconds between ≈ 6000 and ≈ 7000 seconds the “Fermi GBM Orbital Background Subtraction Tool” can not estimate the background at all, due to a SAA passage 30 orbits before or after this time. The high excess of data above the background fit at ≈ 7000 seconds is well visible in the energy channels up to 100 keV in several detectors and will be investigated in the future.